



A generic Hall-Petch relationship in metallic materials with varied grain morphology

Shishir Keerti^{*}, Xinliang Yang^{ORCID}, N. Hari Babu

Brunel Centre for Advanced Solidification Technology, Brunel University of London, Uxbridge, UB8 3PH, United Kingdom

ARTICLE INFO

The Keywords:

Hall-Petch relation
Al binary alloys
Eutectic
Perimeter
Interfacial area

ABSTRACT

The Hall-Petch relationship relates the yield strength (YS) of metallic materials to grain diameter (d), but for alloys with dendritic grains, secondary dendritic arm spacing (λ_2) provides a better fit. This manuscript underscores the significance of considering a perimeter-associated parameter (p'), rather than relying solely on d or λ_2 , to account for strength contribution from morphological changes in various alloys. We propose a generic Hall-Petch relation expressed as $\sigma = \sigma_0 + k'/\sqrt{p'}$, where p' is the area per unit perimeter which can be accurately measured using digital imaging tools and k' is the Hall-Petch constant. To validate this approach, controlled solidification experiments were conducted on Al-Si and Al-Ce alloys across cooling rates from 0.000167 °C/s to 0.34 °C/s. The degree of primary α -Al grain complexity was manipulated through solute additions (Si or Ce), revealing a nonlinear relationship between λ_2 and p' , both experimentally and theoretically. This underscores the critical importance of incorporating the perimeter-associated parameter p' as a fundamental strength metric in the Hall-Petch relation. Hardness changes were analysed alongside evolving grain morphologies. Experimental data from various morphologies (facetted, rosette, dendritic) fit more effectively with the proposed generic Hall-Petch relationship than conventional models.

1. Introduction

Hall and Petch [1,2] independently, observed the influence of grain size on the yield strength (YS) of low carbon steel and iron, following the relation

$$\sigma = \sigma_0 + k/\sqrt{d} \quad (1)$$

where, σ_0 is the stress required to generate dislocation also known as the friction stress, k is the constant known as Hall-Petch (HP hereafter) constant and d is the average diameter of grains. Although widely accepted, this relation is fairly scrutinized [3,4] with the reported value of the average grain diameter's (d) exponent varying from as low as 0.2 to as high as 1, though 1/2 is the most commonly observed value across a broad range of polycrystalline materials.

The Hall-Petch relationship was established on the basis of theoretical framework on the pile up of dislocations against the grain boundary presented by Eshelby et al. [5]. However, several theories have been proposed to explain the physical significance of this relation [6–8] with pile-up theory being the most widely accepted.

In this theory, it is assumed that a dislocation source at the centre of the grain emits multiple dislocations when external load is applied. The grain boundaries act as an obstacle to the movement of these dislocations, resulting in a local stress concentration due to piling up of dislocations, leading to the generation of dislocations in the adjacent grain (Fig. 1(a)).

In HP relationship, the distance between the dislocation source and grain boundary ($d/2$) remains constant. In practicality, non-equiaxed grain morphologies ranging from rosette to dendritic are common in materials, where the distance between dislocation source and the grain boundary spatially varies (Fig. 1(b)) and the parameter d in Eq. (1) needs to be altered to accommodate this effect.

For materials with dendritic grains, HP type empirical relationship between the strength and microstructural features like secondary dendritic arm spacing (λ_2) [9–11], average lamellar spacing [12–14] are reported. Morphology of a grain is known to influence the YS of a material [15,16]. In a comprehensive review article by Cordero et al. [17], the importance of considering grain boundary structure on the grain size strengthening has been highlighted as it still remains a fertile territory for future work. One such attempt is made in a recent study by Jiang

^{*} Corresponding author.

E-mail address: Shishir.Keerti2@brunel.ac.uk (S. Keerti).

et al. [18] by using dislocation dynamics simulation to investigate the effect of three different morphologies of copper grains on the YS. A generalized form of HP relationship was presented incorporating the effect of grain shape through a shape factor associated with the area swept by the dislocation and average dislocation loop length pointing out the importance of grain morphology consideration in grain boundary strengthening.

For a given crystal structure, the morphology of a dendrite is governed by the growth direction. In Al-Zn alloy system, the preferred growth direction of α -Al dendrites is $\langle 100 \rangle$ for up to 25 wt% Zn, and the preferred growth direction changes to $\langle 110 \rangle$ at higher Zn (>60 wt%) [19]. These observations were confirmed by Friedli et al. [20,21] using X-Ray tomography and phase field modelling. Similarly, in Mg-Zn system, Yang et al. [22] used X Ray tomography and EBSD techniques to reveal the changes in morphology of α -Mg with increasing Zn content. At lower solute content (Zn = 0 - 20 wt%) the morphology of α -Mg dendrite changed from 18 branch with growth direction of primary branches $\langle 11 \bar{2} 0 \rangle$ and $\langle 11 \bar{2} 3 \rangle$ to 12 branch with growth direction along $\langle 11 \bar{2} 3 \rangle$ when Zn is more than 40 wt%.

Apart from modifying the microstructure by altering the chemical composition of the alloy, modern external field processing techniques, such as ultrasonic cavitation, high shearing and electromagnetic stirring, are known to produce complex microstructures [23–25]. The complexity in the morphology of a grain can be seen in Table 1, wherein grains with varying morphology and the HP relationship for all cases is presented. For a fully dendritic structure, conventionally, the HP relation is reported to translate into a relation between the YS and λ_2 . Primarily, the distance between the dislocation source and the grain boundary in a dendrite cannot be constant spatially due to the complex morphology, and the stress induced by the piling up of dislocations at the grain boundaries in such complex structures should be dependent on the surface area as higher grain boundary surface area can accommodate higher number of dislocations. The manipulation of grain structure by controlling the processing conditions and composition of an alloy [22, 26,27] raises concerns on the accuracy of λ_2 as the substitute of grain diameter (d) in an alloy with dendritic structure. In two dimensions, the interfacial area concentration of a dendrite has been shown to be represented by the perimeter per unit area [28,29].

Fig. 2 shows a scenario in which an alloy having same λ_2 but with different size of dendrites which resulting in significantly varied interfacial area. This scenario occurs when grain refiner is added [42] and λ_2 based HP type relation doesn't consider this aspect. Similarly, dendrites with same λ_2 can have different morphology depending on the solute content [19] and also presence of nano-particles in the melt can lead to growth of dendrites with varied morphology [43–46]

2. Theoretical aspect - correlation between dendrite perimeter and λ_2

To utilise the interfacial area associated parameter into HP relation, visualization of 3-D structure is required via sophisticated *in situ* measurements [47–50] such as micro CT, high energy X-ray synchrotron facilities etc. It has been confirmed that the interfacial area concentration (ratio of dendrite surface area and its volume) has a similar behaviour with interfacial length concentration (ratio of dendrite perimeter and projected area) [28,29]. Therefore, as a practically viable route, to capture the change in interfacial area induced by the change in morphology of a grain, a two-dimensional inspection can be adopted by measuring the perimeter of dendrite in a unit area of the micrograph which are shown to be equivalent parameters [28]. In the HP relationship, YS is associated with a length scale parameter of the grain diameter (d). To ensure that the new perimeter-associated parameter (p') remains within this length scale and to account for changes in grain morphology in a given area, we consider the ratio of the area of a rectangular envelope enclosing a dendrite to the perimeter of the dendrite. Recent developments in image processing software [51] provides the flexibility and accuracy in making quantitative measurements to capture change in perimeter associated with the morphological changes of a grain.

The 2-D shape of primary and secondary arm tips in a dendrite is conventionally considered as parabolic [52]. Fig. 3 shows a typical dendrite, which can be divided into two parts i.e. primary and secondary arm, for geometrical calculations. The perimeter of the dendrite, p_{total} is formulated in Eqs. (2)–(5) with a and b denoting the primary arm length and width, and c and e denoting the secondary arm length and width, respectively.

$$p_{primary\ arm} = \frac{1}{2} \sqrt{b^2 + 16a^2} + \frac{b^2}{8a} \ln \left(\frac{4a + \sqrt{b^2 + 16a^2}}{b} \right) - \frac{5e}{4} \quad (2)$$

$$p_{secondary\ arm} = \sum_{i=1}^z \sqrt{e^2 + 16c_i^2} + \sum_{i=1}^z \frac{e^2}{4c_i} \ln \left(\frac{4c_i + \sqrt{e^2 + 16c_i^2}}{e} \right) \quad (3)$$

$$c_i = c - \left(\frac{c}{z} \right) (i - 1) \quad (4)$$

$$p_{total} = p_{primary\ arm} + p_{secondary\ arms} \quad (5)$$

$$A = a(2c + b) \quad (6)$$

$$p'_{cal} = \frac{A}{p_{total}} \quad (7)$$

Eq. (4) accounts for varied length scale of secondary arms where z is the

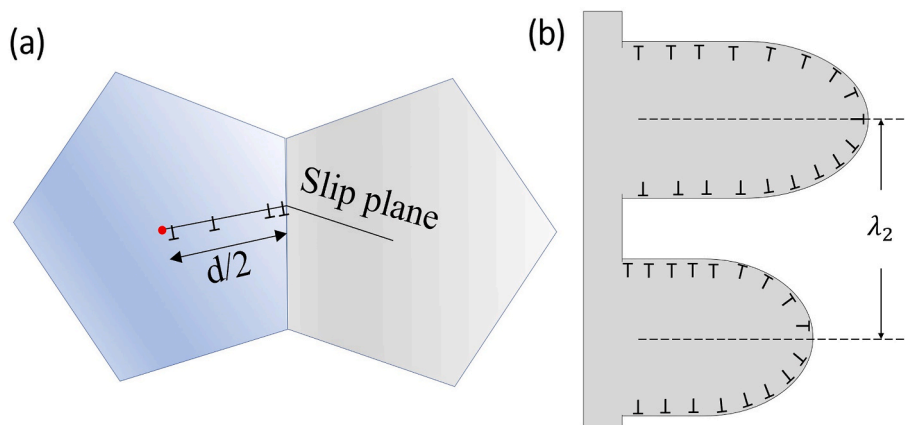
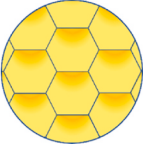
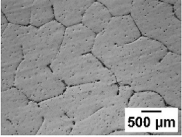
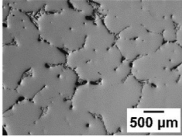
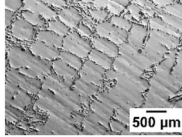
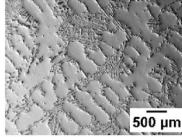
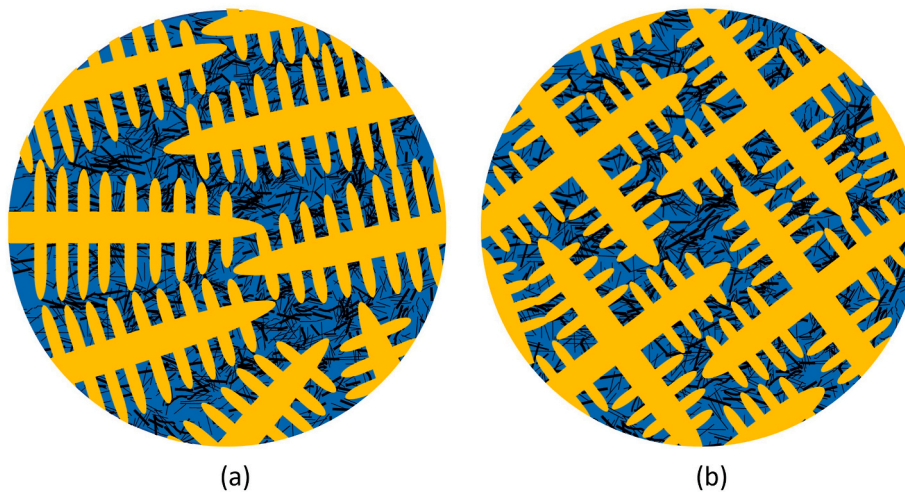


Fig. 1. Illustration of dislocations piling up against the grain boundary in (a) faceted equiaxed grains and (b) dendritic grains in which the length between dislocation source and the grain boundary varies spatially.

Table 1

Illustration of types of microstructures and the corresponding conventional HP type relations in literature.

			
			
Faceted grains (e.g. pure aluminium) $\sigma = \sigma_o + k/\sqrt{d}$ [30–33]	Rosette type grains (e.g. Al-2 wt.% Si alloy) $\sigma = \sigma_o + k/\sqrt{d}$ [34–36]	Rosette-Dendritic (e.g. Al-5 wt.% Si alloy) $\sigma = \sigma_o + k/\sqrt{d}$ [37,38]	Dendritic structure (e.g. Al-8 wt.% Si alloy) $\sigma = \sigma_o + k'/\sqrt{\lambda_2}$ [39–41]

**Fig. 2.** Illustration of dendrites for a given alloy having same λ_2 but with (a) coarse (b) fine dendritic grains.

number of secondary arms in the dendrite. To generate a theoretical data set, a dendrite with a length of 5000 μm , width of 100 μm and the longest secondary arm length of 400 μm is considered. The guideline for selecting these parameters are based on practically observed values for dendrites solidified in gravity die casting solidification condition. The gap between the two consecutive secondary arms is assumed to be 1/4 of the width of an arm i.e. $f = e/4$, which corroborates the measured values of f and e in Al-Si alloys, leading to $\lambda_2 = e + f$, giving $\lambda_2 = 5e/4$. Fig. 4 shows the relationship between the calculated p'_{cal} and λ_2 for the set of dendrites with increasing number of secondary arms from 20 to 300. In this calculation, the length of the primary dendrite a (5000 μm) and the maximum height of secondary arm, $2c + b$ (900 μm) are always kept constant. The ratio between area of the envelope enclosing the dendrite i.e. $A = a(2c + b)$ and p_{total} is the new parameter (p'_{cal}) and its variation with λ_2 is shown in Fig. 4.

The change in λ_2 represents the change in solidification rate and as can be seen in Fig. 4, there exist a non-linear relationship between λ_2 and p'_{cal} in entire range of solidification conditions. The inset shows relationship under practical processing solidification conditions with a consistent non-linearity. This non-linear relationship demands to replace d or λ_2 in HP relation to experimentally measured p' because the dislocation pile-up takes place at the grain boundary and interfacial area occupied by the grain boundary is highly dependent on the morphology of the dendrite structure. In 2-D, this feature can be captured by measuring the p' via measuring the perimeter of a grain from a microstructure using well established image processing tools. The inverse of p'

reflects the degree of complexity of dendritic morphology in a unit area.

To address the morphological changes on the strengthening of the alloy, this work aims to study the correlation between the hardness and perimeter-based parameter (p') associated with the dendritic complexity. In order to study this, we have (i) systematically controlled the solidification rate to affect λ_2 and p' for a given alloy composition, (ii) controlled morphology of the grain via solute (Si, Ce) content at wide range of cooling rates and (iii) used image processing software to measure p' and other microstructural features. To minimize the solid solution and avoid precipitation strengthening contribution, the low solubility elements such as Si (maximum solubility 1.65 wt%) and Ce (maximum solubility 0.0005 wt%) were used to control the grain morphology. To assess the potential change in the preferential growth direction of the α -Al, which in turn affects the HP constant, we have devised the directional solidification for Al-Si alloys with various Si solute content.

3. Experimental procedure

3.1. Samples under controlled growth conditions

To conduct the series of solidification experiments, several large batches (2 kg) of Al-Si alloys with 0, 2, 5, 8, 12.6 wt% Si compositions and Al-5 wt.% Ce alloy were produced in an electrical resistance furnace, by adding appropriate quantities of Al-20 wt% Si and Al-30 wt% Ce master alloys to 99.99 % purity molten aluminium. For each alloy composition T_1 and T_2 in Fig. 5 were chosen to be ($T_{liquidus} + 5^\circ\text{C}$) and

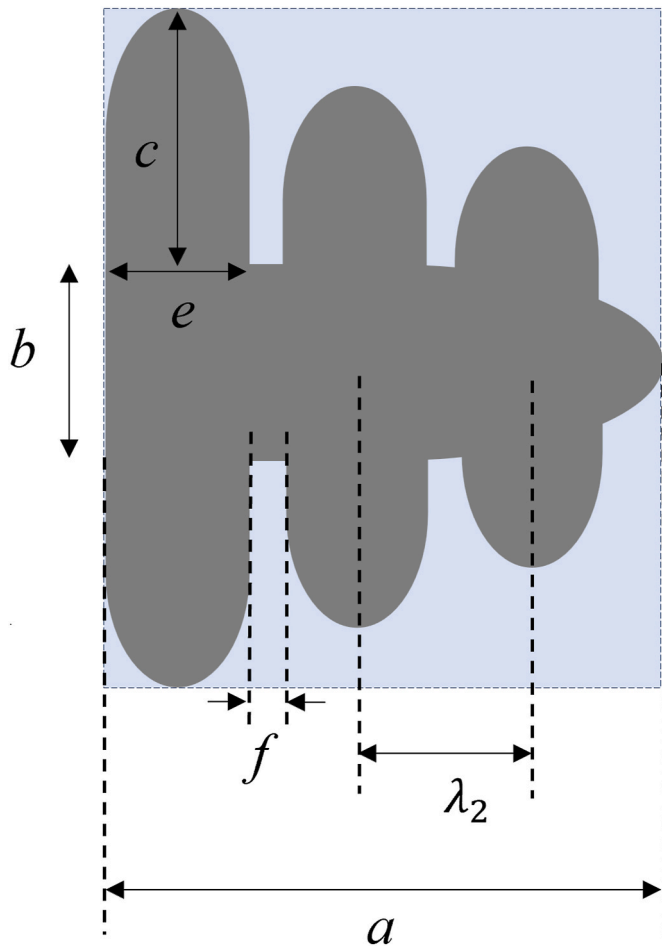


Fig. 3. Illustration of a dendrite.

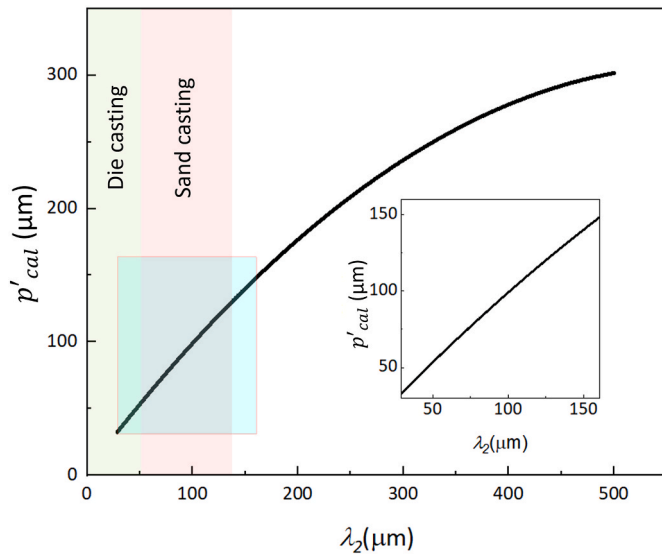


Fig. 4. The relationship between calculated p'_{cal} using Eq. (7) and λ_2 , showing non-linearity in wide range of cooling conditions. Inset shows the consistency of non-linearity in the practical casting conditions.

($T_{\text{eutectic}} - 5^\circ\text{C}$), respectively. The values of T_1 and T_2 for each alloy composition is given in Table 2.

The cooling rate between T_1 and T_2 is precisely controlled by Eurotherm 2416 thermal controller. To minimize temperature fluctuation,

the crucible is placed in thermally insulated assembly and a thermo-couple was placed 2 mm away from melt surface to monitor temperature. The resultant microstructure, shown as in-set Fig. 5, revealing a significant variation in grain size ranging from few centimetres to millimetres. To obtain a sample with a cooling rate of 0.34°C/s , the melt is solidified outside the furnace and the cooling rate is monitored by placing thermo-couple in the melt. In order to enhance the cooling rate further, another solidification experiment was conducted in a copper wedge mould. The cooling rate for three different specific locations were measured to be 10, 48 and 80°C/s and sections of samples from these three locations were used in this study. A summary of alloy compositions and solidification conditions with corresponding cooling rates are presented in Table 3.

3.2. Directional solidification

A refractory material based cylindrical mould, with 15 mm diameter and 40 mm height, was constructed for directional solidification experiments. To eliminate radial heat-dissipation, the mould was wrapped in 5 cm thick insulation material and this assembly was preheated to 10°C higher than the pouring temperature of the liquid metal to establish isothermal condition across the radius. To extract heat directionally from the melt, a cold copper block was inserted at the bottom of cylindrical mould. Once the mould is filled with liquid metal, the top is covered with pre-heated insulating material to minimize heat radiation loss. The macro-etched cross-section, shown in Fig. 17, confirms the columnar growth along vertical thermal gradient driven by directional solidification condition.

3.3. Microstructures and hardness

For macro-etching, ferric chloride was used and for optical microscopy inspections samples were anodized in Barker's reagent (5 mL of 48 % HF with 195 mL of distilled water) for 60–120 s at room temperature. The anodized surface was observed under the polarised light to identify the primary Al grains. The average primary Al grain size was measured as per ASTM E112-13 standard (linear intercept method). The perimeter of the dendrites was measured using the Freehand selection tool, as shown in Fig. 6, in the ImageJ software. To minimize the error in measurements, at least 5 images at different magnifications from each sample were processed, which covered an area of $\sim 600\text{ mm}^2$ in total. Two directional castings were produced for pure Al, Al-2 wt.% Si, Al-5 wt.% Si, Al-8 wt.% Si and Al-12.6 wt.% Si alloys. The samples for EBSD measurements were carefully prepared by standard metallographic process followed by vibration polishing at 100 Hz using Qpol Vibro equipment at 80 % power for 8 h. EBSD analysis of the longitudinal cross section for Al, Al-5 wt.% Si and Al-8 wt.% Si were performed on Zeiss Supra 35 SEM with high sensitivity Hikari EBSD camera (20 kV voltage, 10–15 mm working distance). The data recording and indexing were performed using EDAX Teams software. ATEX software [53] was used for the acquired EBSD data analysis. Examined area for assessing the dendrite growth orientation are $2.8\text{ mm} \times 2.6\text{ mm}$ with step size of $4\ \mu\text{m}$. For hypereutectic alloys, up to 7 locations have been analysed. The misorientation [54] between the $\langle 100 \rangle$ direction and the primary dendrite growth direction is extracted from an average of ~ 30 directionally solidified grains in the longitudinal cross section (solidification direction (SD) - transverse direction (TD)). Brinell hardness tests were conducted with a spherical steel indenter with a diameter 5 mm, at a load of 250 kgf and dwell time of 10 s. On an average, 6 indentations were performed to obtain average Brinell hardness number (BHN) and the standard deviation.

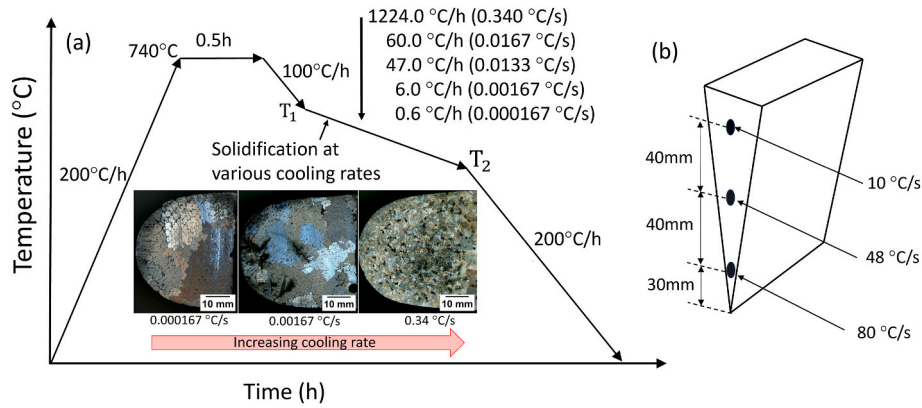


Fig. 5. Schematic of (a) temperature profile used for solidification under controlled cooling conditions, macro etched images for Al-2 wt.% Si are shown for three different cooling rates (b) copper wedge mould showing cooling rate at different positions.

Table 2

Values of T_1 and T_2 for each alloy composition.

Alloy	T_1 (°C)	T_2 (°C)
Al	665	655
Al-2 wt.% Si	653	572
Al-5 wt.% Si	635	572
Al-8 wt.% Si	615	572
Al-12.6 wt% Si	582	572
Al-5 wt.% Ce	657	619

Table 3

Solidification conditions with corresponding cooling rates.

Solidification condition	Alloys investigated	Cooling rate
Controlled cooling	Al, Al-2 wt.% Si, Al-5 wt.% Si, Al-8 wt.% Si, Al-12.6 wt% Si and Al-5 wt.% Ce	1224.0 °C/h (0.340 °C/s)
		60.0 °C/h (0.0167 °C/s)
		47.0 °C/h (0.0133 °C/s)
		6.0 °C/h (0.00167 °C/s)
		0.6 °C/h (0.000167 °C/s)
		0.000167 °C/s
Copper wedge mould	Al-8 wt.% Si	Top 10 °C/s
		Middle 48 °C/s
		Bottom 80 °C/s
		80 °C/s

4. Results and discussion

4.1. Microstructure observation

The morphology of α -Al dendrites (Fig. 7) is observed to be strongly dependent on cooling rate and Si content. For a constant cooling rate of 0.000167 °C/s, the value of λ_2 decreases from 1100 μm to 509 μm when Si content increased from 2 to 8 wt%. This trend was prevalent at other cooling rates as well. The refinement of λ_2 of dendrites with increasing solute content by the virtue of retarded growth velocity due to reduced constitutional undercooling [55,56] is a well discussed phenomenon and is clear in the microstructures. Similar observations were made in Al-5 wt.% Ce alloy (Fig. 8). The measured λ_2 as a function of cooling rate, \dot{T} , is shown in Fig. 9(a) and is well described by $\lambda_2 \propto \dot{T}^{-n}$ relationship, where n is the coarsening exponent, which is reported to be 1/3 [57]. The theoretical approach for the prediction of λ_2 as a function of solute composition and cooling rate was proposed by Kattamis and

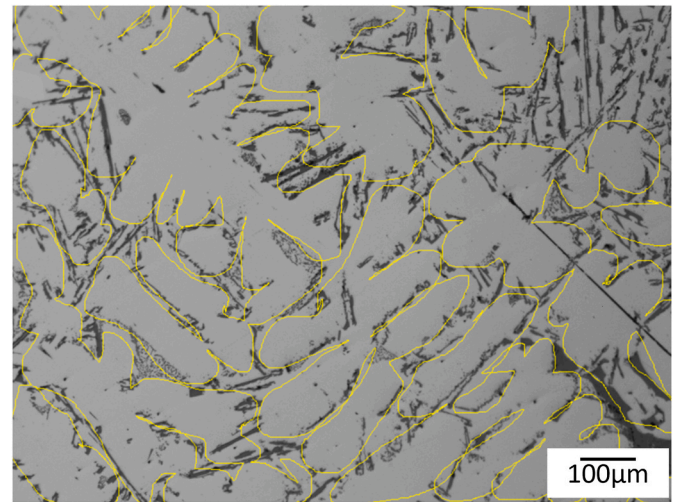


Fig. 6. Freehand tool to measure perimeter of dendrite in ImageJ software.

Fleming [58]. In this model, similar to Oswald ripening, the coarsening of bigger dendritic arm occurs at the expense of thinner secondary dendritic arms. The model posits that the coarsening process is primarily driven by diffusion, as solute atoms migrate from smaller to larger dendritic arms, remelting the thinner dendritic arm and thickening the thicker arm in the process. According to this model [58], λ_2 is given as

$$\lambda_2 = 5.5(Mt_f)^n \quad (8)$$

where

$$M = \frac{-\Gamma D \ln \left[\frac{C_b}{C_o} \right]}{l(1 - k^*)(C_b - C_o)} \quad (9)$$

Where Γ is the Gibbs–Thomson coefficient, D is diffusion coefficient in liquid, l is the slope of liquidus, k^* is partitioning coefficient, C_o is the solute composition and C_b is the composition of the liquid at the base of dendrite which is reached at the solidification time t_f . In a eutectic solidification process, C_b is equal to the eutectic composition.

By substituting $t_f = \Delta T / \dot{T}$ in Eq. (8), where ΔT is the freezing range of the alloys, Eq. (9) can be written as

$$\lambda_2 = M \dot{T}^{-n} \quad (10)$$

where

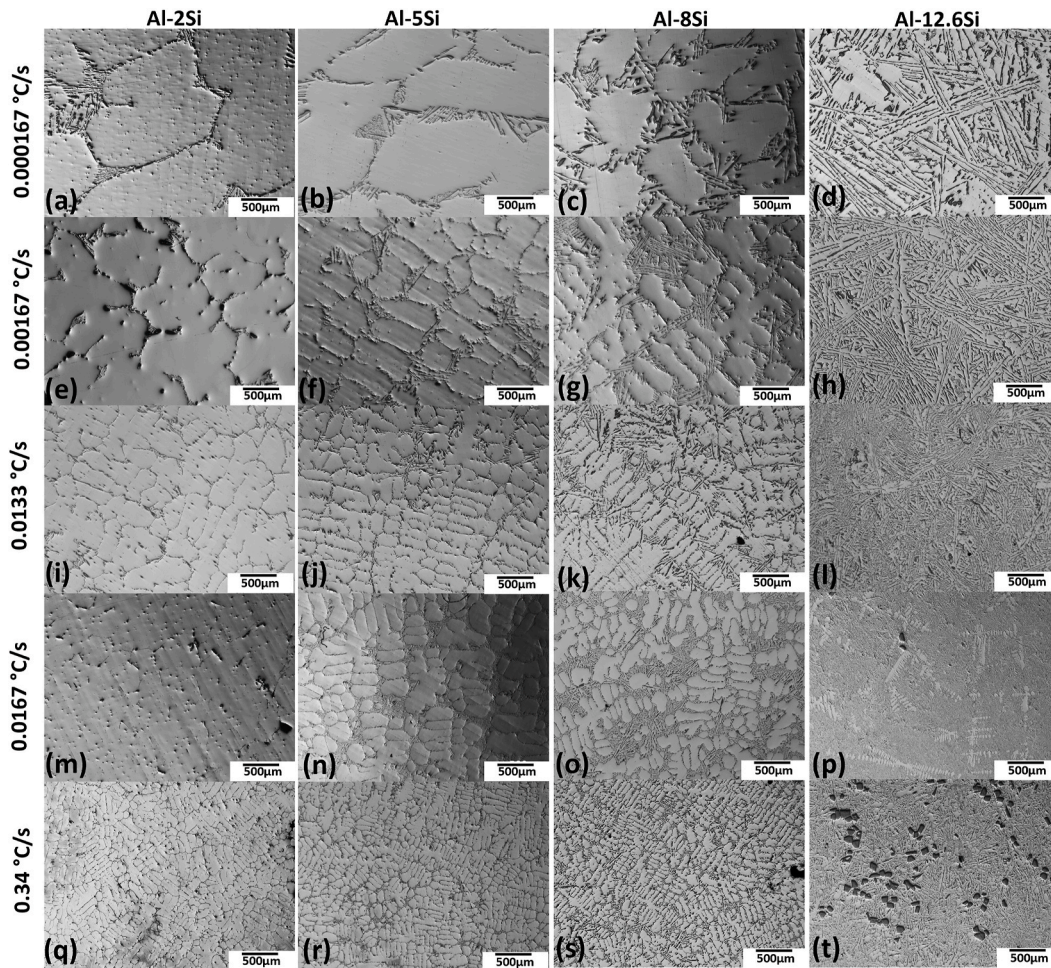


Fig. 7. As cast microstructures of Al-Si binary alloys at several cooling conditions and compositions.

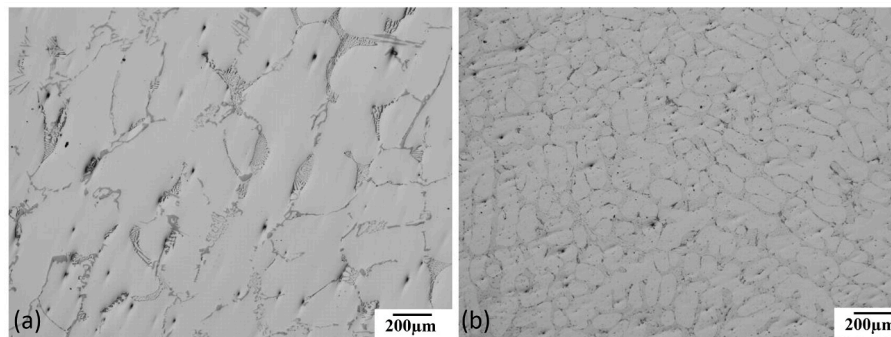


Fig. 8. As cast microstructure of Al-5 wt.% Ce at (a) 0.00167 °C/s and (b) 0.34 °C/s.

$$M = 5.5 \left(\frac{-\Gamma D \ln \left[\frac{C_b}{C_0} \right]}{l(1-k^*)(C_b - C_0)} \Delta T \right)^n \quad (11)$$

The fit parameter M in Eq. (10) as a function of Si content is shown as inset to Fig. 9(a) and agrees with the calculated M values for various Al-Si alloys from Kattamis and Fleming model. As shown in Fig. 9(b), similar to the relationship between λ_2 and \bar{T} , the relationship between p' and \bar{T} is observed to follow $p' \propto \bar{T}^{-m}$. When the experimental data is fitted to the curve with $m = 1/3$, the fit resulted in low regression coefficient (R^2) values (0.82–0.54) for Al-Si alloys. The best fit parameters are

shown in Fig. 9(b) and it is observed that the difference between n and m increases with increasing Si content (Inset to Fig. 9(b)) due to change in morphology from highly dendritic structure at higher solute content to more faceted like structure at lower solute content. At low solute content the value of m approaches the value of n due to near faceted type grains. However, at higher solute content, n and m values deviate noticeably suggesting the importance of considering p' in HP relation rather than d or λ_2 .

In general, eutectic Si morphology is changing from coarse rod to fine needles with increasing cooling rate and their size increases with the increase in Si content. The presence of primary Si at higher cooling rate indicates a shift in the eutectic point [59] in Al-Si alloy. In Al-5 wt.% Ce

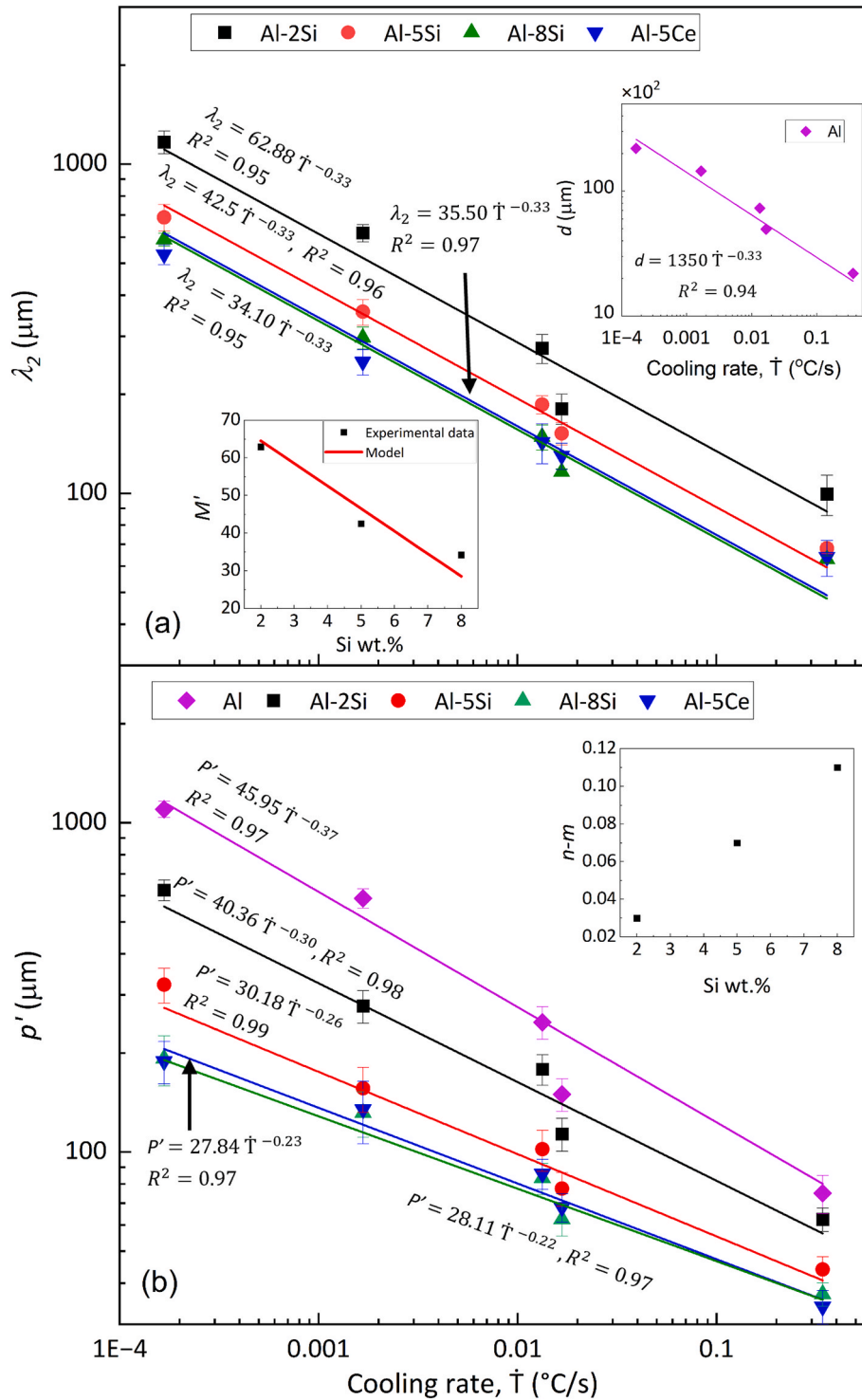


Fig. 9. Variation of (a) λ_2 or d as a function of cooling rate and (b) p' as a function of cooling rate. Inset to Fig. 9(a) shows M' (Kattamis and Fleming model calculations and experimental data) as a function of Si content. Solid lines are the best-fit to $\lambda_2 \propto \dot{T}^{-n}$ and $p' \propto \dot{T}^{-m}$ with the inset of relation between $n-m$ and Si content.

binary alloys, due to negligible solubility of Ce in Al, Ce forms thermally stable intermetallic $\text{Al}_{11}\text{Ce}_3$ in the interdendritic regions. Although it is a strong phase (high in hardness), they fail to translate this strength to the overall strength of the alloy [60]. Lower hardness of the $\text{Al}_{11}\text{Ce}_3$ phase (350HVN) [61], compared to that of silicon (1000HVN) contributes to the lower strength in Al-Ce binary alloys compared to Al-Si alloys.

4.2. Dendrite perimeter

From Fig. 10, it can be noted that the experimentally measured perimeter (p) in a given area is increasing as the solute content increases at all cooling rates studied. The rate of change of perimeter is significant for alloys with higher solute content. This observation coincides with the nonlinear relationship between λ_2 and p'_{cal} . Fig. 11 shows experimentally measured λ_2 and p' for Al-8 wt.% Si alloy solidified under wide range of cooling rates. The data for high cooling rates, in shaded region, were

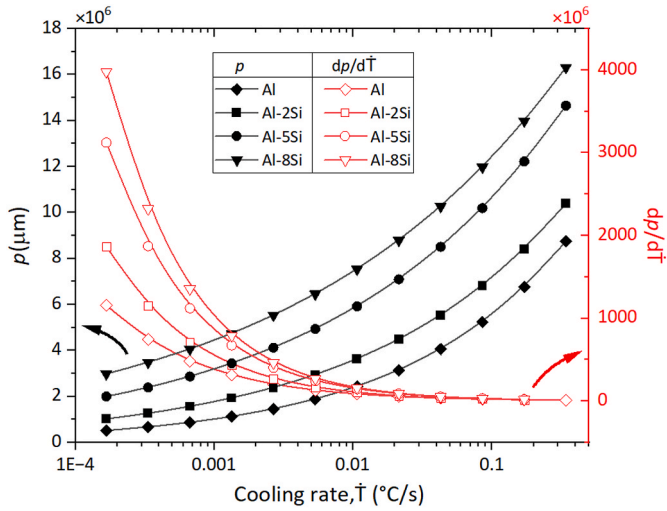


Fig. 10. The perimeter and the rate of change of perimeter as a function of cooling rate for various Al-Si alloy systems.

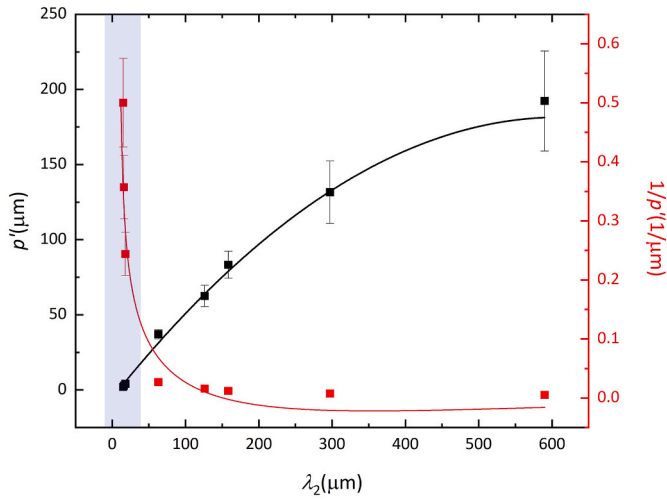


Fig. 11. Relation between experimental p' and λ_2 showing the nonlinearity in Al-8 wt.% Si alloy. For comparison purpose, $1/p'$ vs λ_2 is also plotted. Solid lines are guide to the eye. Shaded region is the data obtained from analysing wedge mould casting.

obtained by analysing the cross sections of samples obtained from Cu based wedge mould cast samples. Rapid change in $1/p'$ vs λ_2 at higher cooling rate (i.e. lower λ_2) indicates that degree of grain complexity changes significantly with small change in λ_2 . As demonstrated in Fig. 4, the non-linearity between the λ_2 and p' persists in the experimental data (Fig. 11) as well and it is the key to relate the strength of a material to the perimeter of the dendrites, which accounts for changes in morphology, rather than λ_2 .

4.3. Correlation between hardness and p'

As shown Fig. 12, the hardness increases with the increasing cooling rate for all studied alloy systems. The hardness of Al-5 wt.% Ce shows a similar trend, rather a sharp increase in the hardness was observed as compared to the Al-Si binary alloys. Since, morphology of $\text{Al}_{11}\text{Ce}_3$ phase changes to a fine lamellar structure with increasing cooling rate, the load bearing capacity by eutectic phase is expected to rise.

In Al-Si alloys, as the hardness is known to linearly related with YS [62–64], here we have measured BHN for all alloys to study the effect of

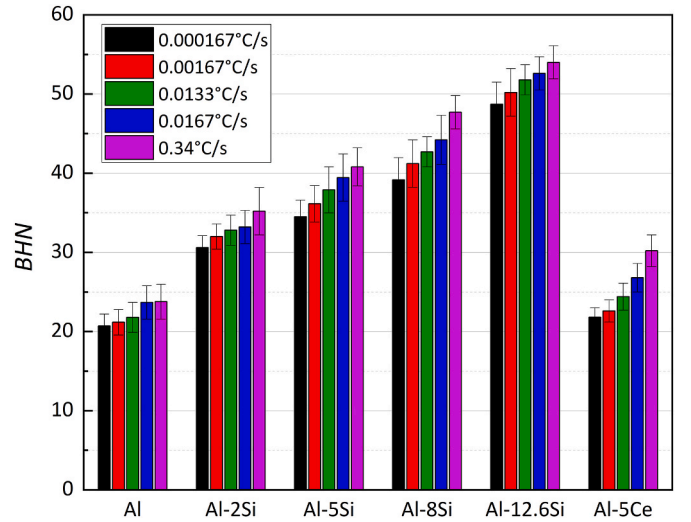


Fig. 12. Brinell hardness of all alloys at several cooling rates.

primary Al grain morphological change on the strengthening of alloy and plotted (Fig. 13) as a function of d , λ_2 and p' for all studied alloys. While the Hall–Petch relationship correlates YS with grain size, hardness testing offers a close estimate of YS, despite limitations arising from localized deformation beneath the indenter. The data is fitted to HP type relations ($BHN = BHN_{o,d} + k/\sqrt{d}$, $BHN = BHN_{o,\lambda_2} + k'/\sqrt{\lambda_2}$, and $BHN = BHN_{o,p'} + k''/\sqrt{p'}$, where $BHN_{o,d}$, BHN_{o,λ_2} , and $BHN_{o,p'}$ are the intercepts and k , k' and k'' are the HP constants). Although at first glance the graphs look similar, the regression coefficients show higher values when p' is considered compared to that of d and λ_2 for all alloys. This demonstrates the importance of considering p' for accounting the changes in strengthening of a material associated with the change in morphology of primary Al grain from spherical to highly dendritic structure. As the grain boundaries pin the dislocations, the higher the grain perimeter per unit area, the higher the accumulation of dislocations.

4.4. Strength contribution from α -Al dendrites

The HP constants, denoted as k' and k'' , exhibit an upward trend as the Si content increases. This phenomenon is likely attributed to variations in the eutectic Si content. The strengthening effect emanating from eutectic colonies is intricately linked to the interlamellar spacing within the eutectic structure. Empirical evidence substantiates that the strength contribution adheres to a HP type relationship [12–14,65], providing experimental validation for this correlation. The hardness of a eutectic system is given by

$$BHN_e = BHN_{o,e} + k_e f_e \lambda_e^{-0.5} \quad (12)$$

Where λ_e is the interlamellar spacing, k_e is the slope of HP type relation with λ , $BHN_{o,e}$ is the intercept and BHN_e is the hardness of the alloy with eutectic composition (Al-12.6 wt% Si), f_e is 1 (the volume fraction of eutectic). λ_e for alloys with eutectic composition of Al-12.6 wt% Si solidified under various cooling rates is measured from microstructures using the method reported in Ref. [66]. To obtain k_e , the BHN data shown in Fig. 12 for Al-12.6 wt% Si alloy, has been fitted to Eq. (12). To extract the hardness contribution associated with the changes in morphology of Al grains, the contribution from eutectic fraction must be subtracted from the overall response of alloy. The hardness response from α -Al matrix is given by

$$BHN_m = BHN - k_e f_e \lambda_j^{-0.5} \quad (13)$$

Where, BHN_m is the contribution in hardness from α -Al dendrites and BHN is the hardness of alloy. λ_j is the interlamellar spacing of eutectic

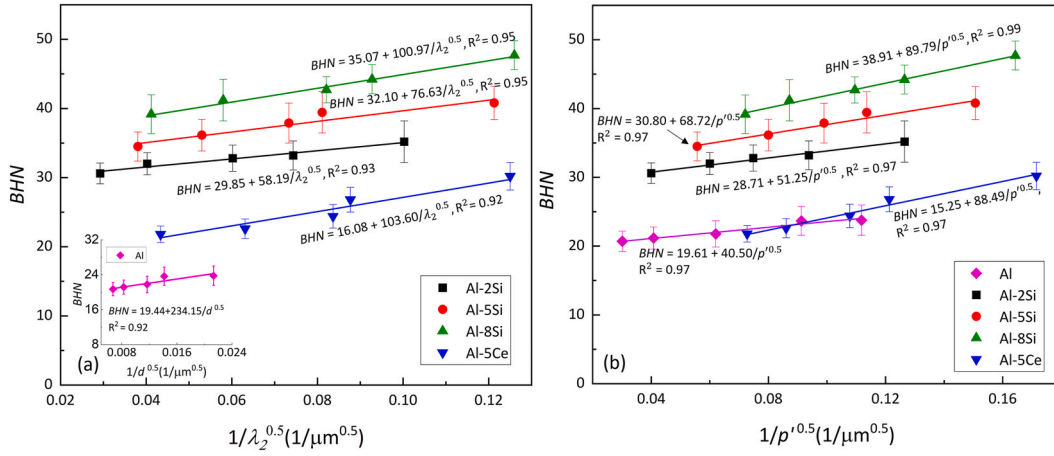


Fig. 13. Relationship between (a) BHN and λ_2 and (b) BHN and p' . Solid lines are linear fit to the HP type relationships.

structure of a hypoeutectic alloy. Experimentally the average interlamellar spacing λ_j is observed to be dependent on the composition and is measured for Al-2 wt.% Si, Al-5 wt.% Si and Al-8 wt.% Si. The true contribution from α -Al to the measured hardness as a function of λ_2 and p' is shown in Fig. 14 and their HP type relationships are given by

$$BHN_m = BHN'_{o,\lambda_2} + k'_m \lambda_2^{-0.5} \tag{14}$$

$$BHN_m = BHN'_{o,p'} + k''_m p'^{-0.5} \tag{15}$$

where BHN'_{o,λ_2} and $BHN'_{o,p'}$ are intercepts; k'_m and k''_m are the HP constants. The R^2 values (given in Fig. 14) shows higher value when p' is considered in HP relation when compared to that of d or λ_2 for all alloys. This again demonstrates that it is important to consider p' for accounting the changes in strengthening of a material associated with the change in morphology of primary Al grain from spherical to highly dendritic structure. To reiterate the importance of considering perimeter for practical commercial Al-Si alloy, data for Al-8 wt.% Si (a typical practical cast alloy) is shown in Fig. 15, where R^2 is observed to improve from 0.93 to 0.98 which is very significant change from practical application view point.

To illustrate changes in hardness associated with friction stress of a matrix, both BHN and BHN_m data has been plotted in Fig. 16. Two distinct observations can be made from this graph, firstly the effect of Si on the intercept i.e. $BHN'_{o,p'}$ for Al-Si alloys is higher than that of pure Al even after removing the hardness contribution from the eutectic fraction and secondly the slope, i.e. k''_m increases with the Si content.

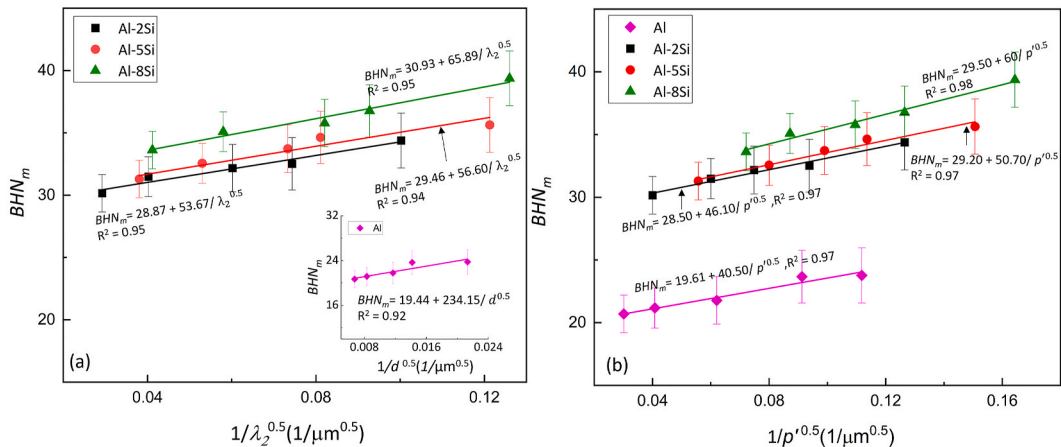


Fig. 14. Relationship between (a) BHN_m and λ_2 and (b) BHN_m and p' . The solid lines are fits to the HP relationships given in Eqs. (14) and (15).

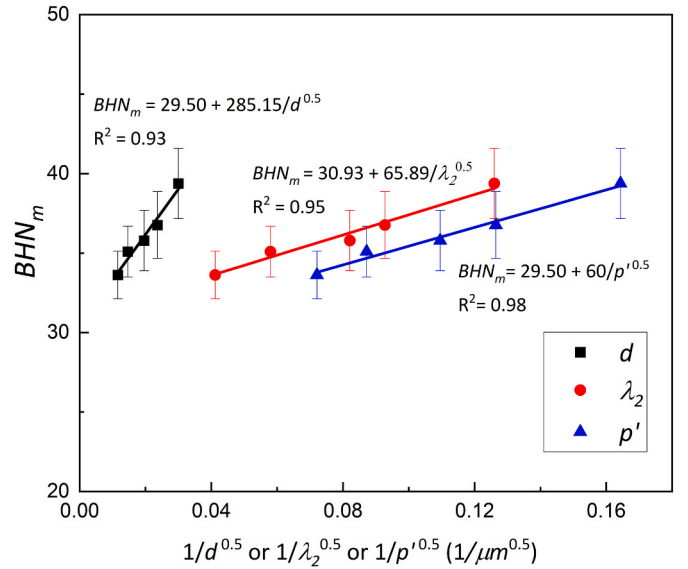


Fig. 15. HP type relationships [BHN_m vs p' ; BHN_m vs λ_2 ; BHN_m vs d] for Al-8 wt.% Si alloy solidified at various cooling rates. The legends are experimental data and the solid lines are linear fit.

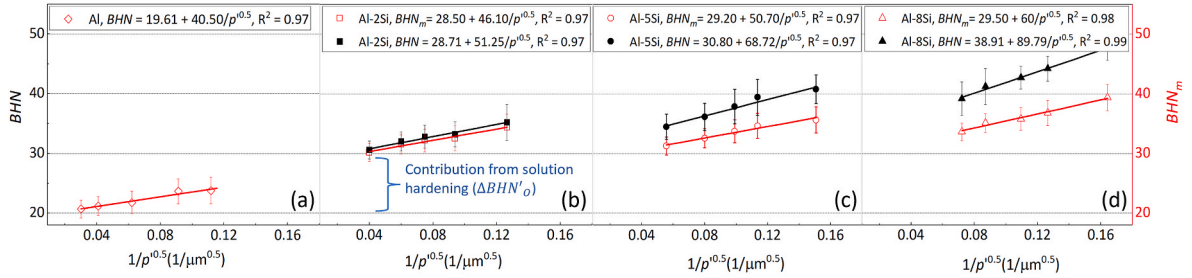


Fig. 16. HP type relationships [BHN_m vs p' and BHN vs p'] for all Al-Si alloy systems. A significant increase in intercept due to solid solution strengthening contribution to the hardness can be clearly seen. Increase in k'_m value with the increased Si content can also be seen.

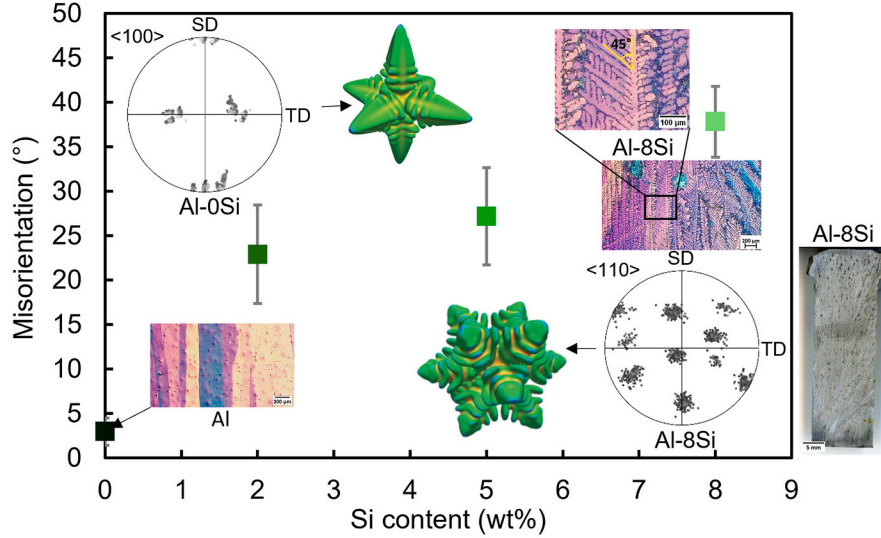


Fig. 17. Plot showing the variation of angle between the α -Al growth direction and the principal crystal axis as a function of Si content in directional solidified samples. A photograph of macro-etched cross-section of directionally solidified Al-8 wt.% Si sample reveal columnar growth induced by directional solidification. The optical micrographs from anodized samples showing columnar grains as well as change in grain morphology as a consequence of solute presence. Pole figure analysis on columnar grains, shown as inset, reveals the dendrite orientation transition from $\langle 100 \rangle$ for Al to $\langle 110 \rangle$ for Al-8 wt.% Si alloys. For Al-8 wt.% Si alloy, 45° side branching within the columnar dendrite can be observed in the microstructure. Examples of equiaxed grains with $\langle 100 \rangle$ and $\langle 110 \rangle$ growth orientations generated from phase field is reprinted from Ref. [21].

The friction stress σ_o in Eq. (1), represented by the intercept on y-axis of HP relationship plot, has several components [67]

$$\sigma_o = \sigma_{CRSS} + \sigma_p + \Delta\sigma_{ss} \quad (16)$$

Where, σ_{CRSS} is the critical resolved shear stress, $\Delta\sigma_{ss}$ is the improvement due to solid solution and σ_p is the residual stress due to the dislocations associated with thermomechanical processing.

The first component of friction stress, i.e. σ_{CRSS} is known to depend on the slip system activated during deformation. The number of active slip systems during mechanical test is dependent on the grain orientation and loading direction. Generally, slip systems with higher Schmid factor requires small applied stress to initiate slip. Compression [68], tensile [69,70] tests on Al single crystal showed higher YS for crystals with $[111]$ orientation than that of $[100]$ and $[110]$ orientations. In as cast polycrystalline material, the grains are randomly oriented with respect to applied load and therefore the σ_{CRSS} contribution remains unaffected for all studied alloys. Although thermomechanical processing can have a significant effect on σ_o in Al alloys [71], the current study focuses on the as-cast condition and no plastic deformation from thermomechanical processing is involved, the dislocation density related component σ_p is minimal and can be neglected in these as-cast samples.

The third component $\Delta\sigma_{ss}$ in Eq. (16), can be predicted by Fleischer model [72]

$$\Delta\sigma_{ss} = LGb\epsilon_{ss}^{3/2}\sqrt{c_s} \quad (17)$$

where, L is orientation factor which is 3.06 for FCC material, G is shear modulus (25 GPa), b is Burgers vector (0.28 nm), c_s is the atomic solute concentration and ϵ_{ss} is the lattice strain, which can be given by

$$\epsilon_{ss} = |\epsilon'_G - \beta\epsilon_b| \quad (18)$$

Where ϵ'_G is the modulus mismatch parameter and is given by

$$\epsilon'_G = 1/1 + 0.5\epsilon_G \quad (19)$$

And ϵ_G is the modulus mismatch and ϵ_b is the strain mismatch due to difference in atomic radii of solute and matrix atoms.

Eq. (17) leads to a value of $\Delta\sigma_{ss} = 2.5$ MPa which equates to Vickers hardness number (HVN) of 8 based on the relationship between HVN and σ for Al-Si binary alloy [73]. The enhanced BHN'_o ($\Delta BHN'_o$ shown in Fig. 16(b)), when 2% Si is added to Al, is originated from solid solution formation, which has been reported elsewhere [74,75].

By introducing 2 wt% Si in Al, in addition to increase in BHN'_o , the HP constant (k'_m) value is observed to increase, which can also be attributed to the Si solute in Al matrix as the experimental conditions are far from the equilibrium solidification conditions. For multicomponent alloys, Toda-Caraballo et al. [67] have proposed a general expression for

HP constant as a function of solute content and it is given by

$$k = k_{Al} + \sum X_i \Delta k \quad (20)$$

Where, k_{Al} is the HP constant for Al matrix and X_i is the solute content and $\Delta k = (\vartheta \Delta G + \gamma \Delta b)$, where ϑ and γ are constants dependent on the magnitude of Burger vector b and shear modulus G [67]. From Eq. (20) it is clear that k is strongly dependent on the solute content, ΔG and Δb . The change in HP constant as function of solute content has been observed [35,76] in Mg-Zn system and Toda-Caraballo et al. [67] have successfully fitted the experimental data with Eq. (20). Since, the solubility of Si in Al is ≤ 1.65 wt%, based on Eq. (20), k_m' should not increase for samples beyond 1.65 wt% of Si addition. However, as shown in Fig. 16(c) and (d), increase in k_m' is still noticeable in alloys with 5 wt% and 8 wt% Si.

4.5. Influence of dendrite growth direction on Hall-Petch constant

Several studies [77,78] have attributed the change in HP constant, on the active deformation modes which are dependent on the grain orientation and loading direction. In HCP materials, thermomechanical processing is observed to alter the crystallographic texture [79] which affects the k value [80–82] significantly. For instance, k value measured under tension for friction stir processed AZ31 magnesium alloy was 160 MPa $\mu\text{m}^{1/2}$, whereas, for its hot extruded counterparts, k value was 303 MPa $\mu\text{m}^{1/2}$ [83]. In another study, the variation of k value from 228 to 158 and 411 MPa $\mu\text{m}^{1/2}$ was observed, when the tension direction varies from 0° to 45° and 90° away from the normal direction of a hot-rolled AZ31 plate [81], respectively. In FCC materials, although relatively lesser studies are available, this effect was reported in electrodeposited Ni with different grain orientations [84]. In the current study, no specific effort was made to alter orientation of grains and the grains are expected to be randomly oriented. The only variable in present study is the solute content and solute induced dendrite orientation transition (DOT) is known to occur in Al and Mg alloys due to the weak anisotropy of solid-liquid interfacial energy [19,22,85,86]. Gonzales et al. [85] have observed change in the growth morphology of Al from $\langle 100 \rangle$ to $\langle 110 \rangle$ growth directions as Zn content was increased from 25 wt% to 60 wt%. Similar observations were made in Al-Ge systems, where primary dendrite arms were found to be growing in $\langle 100 \rangle$ direction in Al-20 wt% Ge alloys, $\langle 110 \rangle$ direction in Al-46 wt% Ge, and both $\langle 100 \rangle$ and $\langle 110 \rangle$ directions growing simultaneously at an intermediate composition of Al-29 wt% Ge [87].

As can be seen in Fig. 17, for pure Al sample, the measured growth direction is consistent with reported $\langle 100 \rangle$ [86], whereas with increasing Si content, the preferred growth orientation has deviated progressively from $\langle 100 \rangle$ to close to $\langle 110 \rangle$ in Al-8 wt.% Si alloy. Though the permanent mould casting employed here to investigate HP-type relation leads to randomly oriented grains, however, the preferential growth of individual dendrite will follow the tendency presented in Fig. 17 in which the Si content has strong influence on preferential growth direction.

Dislocation dynamics simulation on the textured FCC grains [18] with different morphologies has been confirmed to affect the HP constant strongly. On the other hand, the reported HP-type relation in this study is analysed based on randomly oriented bulk material. Although to our best knowledge the effect of change in dendritic growth direction on the HP constant in such situation is not reported in literature, based on the theoretical study from Jiang et al. [18], it is likely to affect k values.

5. Conclusions

Hall and Petch observed that the difference between the flow stress of a polycrystal and that of a single crystal is directly proportional to the inverse of the square root of the average grain diameter. Over the last six decades, this relationship has undergone extensive discussion across a

spectrum of metallic materials and has found application in computational alloy design approaches. The distance between the dislocation source and the grain boundary is deemed to be half the diameter of the average grain size. Given that non-equiaxed grain morphologies, ranging from rosette to dendritic, are prevalent in materials where the distance between the dislocation source and the grain boundary radially varies, our manuscript underscores the significance of introducing a perimeter-associated parameter to accommodate changes in grain morphology. We have proposed a generic Hall-Petch relation $\sigma = \sigma_0 + k'/\sqrt{p'}$, wherein p' represents the area per unit perimeter, a parameter that can be accurately measured experimentally using digital image processing tools. To validate this, a series of Al-Si and Al-Ce binary alloys with a range of dendritic morphologies were synthesized and analysed. The key conclusions are as follows:

- For dendritic grain morphology, p' exhibits a nonlinear relationship with λ_2 over a broad range of cooling rates, substantiated both mathematically and experimentally. This non-linearity becomes more pronounced with the increasing complexity of dendritic structures, underscoring the importance of considering grain perimeter in predicting YS.
- The generic Hall-Petch type relationship yields a superior coefficient of regression (>0.97) for alloys with diverse grain morphologies compared to the conventional Hall-Petch relationship, which relies on either d or λ_2 .
- The Hall-Petch constant is observed to increase with rising Si content, attributed to the shift in the preferential growth direction of α -Al dendrites from $\langle 001 \rangle$ to $\langle 110 \rangle$ when Si concentration increases to 8 wt%.

This enhanced generic Hall-Petch relation offers a more accurate and comprehensive description of the intricate interplay between grain morphology complexity and material strength. As modern image processing tools can precisely measure grain perimeters, incorporating this generic relation into computational alloy design approaches holds promise for enhancing accuracy.

CRediT authorship contribution statement

Shishir Keerti: Writing – original draft, Methodology, Investigation, Formal analysis, Data curation. **Xinliang Yang:** Writing – review & editing, Validation, Methodology, Investigation, Formal analysis, Data curation. **N. Hari Babu:** Writing – review & editing, Visualization, Validation, Supervision, Resources, Methodology, Funding acquisition, Conceptualization.

Declaration of competing interest

The authors declare the following financial interests/personal relationships which may be considered as potential competing interests: Hari Babu Nadendla reports financial support was provided by Engineering and Physical Sciences Research Council. If there are other authors, they declare that they have no known competing financial interests or personal relationships that could have appeared to influence the work reported in this paper.

Acknowledgment

The authors wish to acknowledge financial support from the Engineering and Physical Sciences Research Council project (EP/Y025016/1).

Data availability

Data will be made available on request.

References

- [1] N.J. Petch, The cleavage strength of polycrystals, *J. Iron Steel Inst.* 174 (1953) 25–28.
- [2] E.O. Hall, The deformation and ageing of mild steel: III discussion of results, *Proc. Phys. Soc. B* 64 (1951) 747–753, <https://doi.org/10.1088/0370-1301/64/9/303>.
- [3] D.J. Dunstan, A.J. Bushby, Grain size dependence of the strength of metals: the Hall-Petch effect does not scale as the inverse square root of grain size, *Int. J. Plast.* 53 (2013) 56–65, <https://doi.org/10.1016/j.ijplas.2013.07.004>.
- [4] Y. Li, A.J. Bushby, D.J. Dunstan, The Hall-Petch effect as a manifestation of the general size effect, *Proc. R. Soc. A* 472 (2016), <https://doi.org/10.1098/rspa.2015.0890>.
- [5] J.D. Eshelby, F.C. Frank, F.R.N. Nabarro, XLI. The equilibrium of linear arrays of dislocations, London, Edinburgh Dublin Phil. Mag. J. Sci. 42 (1951) 351–364, <https://doi.org/10.1080/14786445108561060>.
- [6] M.F. Ashby, The deformation of plastically non-homogeneous materials, *Philos. Mag.* 21 (1970) 399–424, <https://doi.org/10.1080/14786437008238426>.
- [7] E. Smith, P.J. Worthington, The effect of orientation on the grain size dependence of the yield strength of metals, *Philos. Mag.* 9 (1964) 211–216, <https://doi.org/10.1080/14786436408229186>.
- [8] M.A. Meyers, E. Ashworth, A model for the effect of grain size on the yield stress of metals, *Philos. Mag.* A 46 (1982) 737–759, <https://doi.org/10.1080/01418618208236928>.
- [9] E.C. Araújo, A.S. Barros, R.H. Kikuchi, A.P. Silva, F.A. Gonçalves, A.L. Moreira, O. L. Rocha, The role of Si and Cu alloying elements on the dendritic growth and microhardness in horizontally solidified binary and multicomponent aluminum-based alloys, *Metall. Mater. Trans.* 48 (2017) 1163–1175, <https://doi.org/10.1007/s11661-016-3942-4>.
- [10] W.R. Osório, C.A. Santos, J.M.V. Quesma, A. Garcia, Mechanical properties as a function of thermal parameters and microstructure of Zn-Al castings, *J. Mater. Process. Technol.* (2003) 703–709, [https://doi.org/10.1016/S0924-0136\(03\)00355-8](https://doi.org/10.1016/S0924-0136(03)00355-8).
- [11] W.R. Osório, P.R. Goulart, G.A. Santos, C.M. Neto, A. Garcia, Effect of dendritic arm spacing on mechanical properties and corrosion resistance of Al 9 Wt pct Si and Zn 27 Wt pct Al alloys, *Metall. Mater. Trans.* A 37 (2006) 2525–2538, <https://doi.org/10.1007/BF02586225>.
- [12] P. Pandey, S.K. Makineni, B. Gault, K. Chattopadhyay, On the origin of a remarkable increase in the strength and stability of an Al rich Al-Ni eutectic alloy by Zr addition, *Acta Mater.* 170 (2019) 205–217, <https://doi.org/10.1016/j.actamat.2019.03.025>.
- [13] R. Kakitani, R.V. Reyes, A. Garcia, J.E. Spinelli, N. Cheung, Relationship between spacing of eutectic colonies and tensile properties of transient directionally solidified Al-Ni eutectic alloy, *J. Alloys Compd.* 733 (2018) 59–68, <https://doi.org/10.1016/j.jallcom.2017.10.288>.
- [14] L. Wang, B. Ye, W. Huang, W. Ding, Theoretical model of yield strength for eutectic colony microstructure materials, *Scr. Mater.* 231 (2023), <https://doi.org/10.1016/j.scriptamat.2023.115443>.
- [15] P. Van Houtte, On the equivalence of the relaxed Taylor theory and the Bishop-Hill theory for partially constrained plastic deformation of crystals, *Mater. Sci. Eng.* 55 (1982) 69–77, [0.1016/0025-5416\(82\)90085-4](https://doi.org/10.1016/0025-5416(82)90085-4).
- [16] L. Delannay, M.R. Barnett, Modelling the combined effect of grain size and grain shape on plastic anisotropy of metals, *Int. J. Plast.* 32–33 (2012) 70–84, <https://doi.org/10.1016/j.ijplas.2011.12.002>.
- [17] Z.C. Cordero, B.E. Knight, C.A. Schuh, Six decades of the Hall–Petch effect – a survey of grain-size strengthening studies on pure metals, *Int. Mater. Rev.* 61 (2016) 495–512, <https://doi.org/10.1080/09506608.2016.1191808>.
- [18] M. Jiang, B. Devincere, G. Monnet, Effects of the grain size and shape on the flow stress: a dislocation dynamics study, *Int. J. Plast.* 113 (2019) 111–124, <https://doi.org/10.1016/j.ijplas.2018.09.008>.
- [19] T. Haxhimali, A. Karma, F. Gonzales, M. Rappaz, Orientation selection in dendritic evolution, *Nat. Mater.* 5 (2006) 660–664, <https://doi.org/10.1038/nmat1693>.
- [20] J. Friedli, J.L. Fife, P. Di Napoli, M. Rappaz, X-ray tomographic microscopy analysis of the dendrite orientation transition in Al-Zn, in: *IOP Conf Ser Mater Sci Eng.* 2012, <https://doi.org/10.1088/1757-899X/33/1/012034>.
- [21] J. Friedli, P. Di Napoli, M. Rappaz, J.A. Dantzig, Phase-field modeling of the dendrite orientation transition in Al-Zn alloys, in: *IOP Conf Ser Mater Sci Eng.* 2012, <https://doi.org/10.1088/1757-899X/33/1/012111>.
- [22] M. Yang, S.M. Xiong, Z. Guo, Effect of different solute additions on dendrite morphology and orientation selection in cast binary magnesium alloys, *Acta Mater.* 112 (2016) 261–272, <https://doi.org/10.1016/j.actamat.2016.04.014>.
- [23] G. Wang, M.S. Dargusch, M. Qian, D.G. Eskin, D.H. StJohn, The role of ultrasonic treatment in refining the as-cast grain structure during the solidification of an Al-2Cu alloy, *J. Cryst. Growth* 408 (2014) 119–124, <https://doi.org/10.1016/j.jcrysgro.2014.09.018>.
- [24] H.T. Li, M. Xia, P. Jarry, G.M. Scamans, Z. Fan, Grain refinement in an AlZnMgCuTi alloy by intensive melt shearing: a multi-step nucleation mechanism, *J. Cryst. Growth* 314 (2011) 285–292, <https://doi.org/10.1016/j.jcrysgro.2010.10.168>.
- [25] M. Qian, A. Ramirez, An approach to assessing ultrasonic attenuation in molten magnesium alloys, *J. Appl. Phys.* 105 (2009), <https://doi.org/10.1063/1.3054374>.
- [26] M.A. Easton, H. Kaufmann, W. Fragner, The effect of chemical grain refinement and low superheat pouring on the structure of NRC castings of aluminium alloy Al-7Si-0.4Mg, *Mater. Sci. Eng.* 420 (2006) 135–143, <https://doi.org/10.1016/j.msea.2006.01.078>.
- [27] J.C. Jie, S.P. Yue, J. Liu, D.H. StJohn, Y.B. Zhang, E.Y. Guo, T.M. Wang, T.J. Li, Revealing the mechanisms for the nucleation and formation of equiaxed grains in commercial purity aluminum by fluid-solid coupling induced by a pulsed magnetic field, *Acta Mater.* 208 (2021), <https://doi.org/10.1016/j.actamat.2021.116747>.
- [28] Q. Li, C. Beckermann, Scaling behavior of three-dimensional dendrites, *Phys. Rev. E* 57 (1998) 3176–3188, <https://doi.org/10.1103/PhysRevE.57.3176>.
- [29] E. Hurlimann, R. Trittbach, U. Bisang, J.H. Bilgram, Integral parameters of xenon dendrites, *Phys. Rev. A (Coll Park)* 46 (1992) 6579–6595, <https://doi.org/10.1103/PhysRevA.46.6579>.
- [30] M. Furukawa, Z. Horita, M. Nemoto, R.Z. Valiev, T.G. Langdon, Microhardness measurements and the Hall-Petch relationship in an Al Mg alloy with submicrometer grain size, *Acta Mater.* 44 (1996) 4619–4629, [https://doi.org/10.1016/1359-6454\(96\)00105-X](https://doi.org/10.1016/1359-6454(96)00105-X).
- [31] S. Yoshida, T. Ikeuchi, T. Bhattacharjee, Y. Bai, A. Shibata, N. Tsuji, Effect of elemental combination on friction stress and Hall-Petch relationship in face-centered cubic high/medium entropy alloys, *Acta Mater.* 171 (2019) 201–215, <https://doi.org/10.1016/j.actamat.2019.04.017>.
- [32] T. Huang, L. Shuai, A. Wakeel, G. Wu, N. Hansen, X. Huang, Strengthening mechanisms and Hall-Petch stress of ultrafine grained Al-0.3%Cu, *Acta Mater.* 156 (2018) 369–378, <https://doi.org/10.1016/j.actamat.2018.07.006>.
- [33] S. Nagarjuna, M. Srinivas, K.K. Sharma, The grain size dependence of flow stress in a Cu-26Ni-17Zn alloy, *Acta Mater.* 48 (2000) 1807–1813, [https://doi.org/10.1016/S1359-6454\(99\)00464-4](https://doi.org/10.1016/S1359-6454(99)00464-4).
- [34] J.P. Weiler, J.T. Wood, R.J. Klassen, R. Berkmortel, G. Wang, The effect of grain size on the flow stress determined from spherical microindentation of die-cast magnesium AM60B alloy, *J. Mater. Sci.* (2005) 5999–6005, <https://doi.org/10.1007/s10853-005-1295-2>.
- [35] C.H. Caceres, G.E. Mann, J.R. Griffiths, Grain size hardening in Mg and Mg-Zn solid solutions, *Metall. Mater. Trans. A Phys. Metall. Mater. Sci.* 42 (2011) 1950–1959, <https://doi.org/10.1007/s11661-010-0599-2>.
- [36] M.A. Herbert, C. Sarkar, R. Mitra, M. Chakraborty, Microstructural evolution, hardness, and alligating in the Mushy state rolled cast Al-4.5Cu alloy and In-situ Al4.5Cu-5TiB2 composite, *Metall. Mater. Trans. A Phys. Metall. Mater. Sci.* 38 A (2007) 2110–2126, <https://doi.org/10.1007/s11661-007-9264-9>.
- [37] M. Maleki, F. Jamei, M. Emamy, H. Mirzadeh, Microstructure and mechanical properties of as-cast and wrought Mg-Ni in-situ formed alloys, *Mater. Sci. Technol.* (2022), <https://doi.org/10.1080/02670836.2022.2154934>.
- [38] H.M. Guo, A. sheng Zhang, B. Hu, Y. Ding, X.B. Liu, Refining microstructure of AZ91 magnesium alloy by introducing limited angular oscillation during initial stage of solidification, *Mater. Sci. Eng.* 532 (2012) 221–229, <https://doi.org/10.1016/j.msea.2011.10.083>.
- [39] J. Wang, Y. Liu, J. Zhu, Y. Liu, X. Su, Effect of complex modification on microstructure and mechanical properties of hypoeutectic Al–Si, *Metallogr. Microstruct. Anal.* 8 (2019) 833–839, <https://doi.org/10.1007/s13632-019-00584-7>.
- [40] LiaoYu Hengcheng, SunGuoxiong Sun, Correlation between mechanical properties and amount of dendritic a-Al phase in as-cast near-eutectic Al–11.6% Si alloys modified with strontium, *Mater. Sci. Eng.* 335 (2002) 62–66, [https://doi.org/10.1016/S0921-5093\(01\)01949-9](https://doi.org/10.1016/S0921-5093(01)01949-9).
- [41] B.P. Reis, M.M. Lopes, A. Garcia, C.A. dos Santos, The correlation of microstructure features, dry sliding wear behavior, hardness and tensile properties of Al-2wt%Mg-Zn alloys, *J. Alloys Compd.* 764 (2018) 267–278, <https://doi.org/10.1016/j.jallcom.2018.06.075>.
- [42] L. Bolzoni, M. Nowak, N. Hari Babu, Grain refinement of Al-Si alloys by Nb-B inoculation. Part II: application to commercial alloys, *Mater. Des.* 66 (2015) 376–383, <https://doi.org/10.1016/j.matdes.2014.08.067>.
- [43] L. Gránásy, T. Pusztai, T. Börzsönyi, J.A. Warren, J.F. Douglas, A general mechanism of polycrystalline growth, *Nat. Mater.* 3 (2004) 645–650, <https://doi.org/10.1038/nmat1190>.
- [44] R. Daudin, S. Terzi, P. Lhuissier, J. Tamayo, M. Scheel, N. Hari Babu, D.G. Eskin, L. Salvo, Particle-induced morphological modification of Al alloy equiaxed dendrites revealed by sub-second in situ microtomography, *Acta Mater.* 125 (2017) 303–310, <https://doi.org/10.1016/j.actamat.2016.12.005>.
- [45] Enyu Guo, Sansan Shuai, Daniil Kazantsev, Shyamprasad Karagadde, A.B. Phillion, Tao Jing, Wenzhen Li, Peter D. Lee, The influence of nanoparticles on dendritic grain growth in Mg alloys, *Acta Mater.* 152 (2018) 127–137, <https://doi.org/10.1016/j.actamat.2018.04.023>.
- [46] L. Gránásy, T. Pusztai, J.A. Warren, J.F. Douglas, T. Börzsönyi, V. Ferreiro, Growth of “dizzy dendrites” in a random field of foreign particles, *Nat. Mater.* 2 (2003) 92–96, <https://doi.org/10.1038/nmat815>.
- [47] N. Limodin, L. Salvo, E. Boller, M. Suéry, M. Felberbaum, S. Gaillègue, K. Madi, In situ and real-time 3-D microtomography investigation of dendritic solidification in an Al-10 wt.% Cu alloy, *Acta Mater.* 57 (2009) 2300–2310, <https://doi.org/10.1016/j.actamat.2009.01.035>.
- [48] O. Ludwig, M. Dimichiel, L. Salvo, M. Suéry, P. Falus, In-situ three-dimensional microstructural investigation of solidification of an Al-Cu alloy by ultrafast X-ray microtomography, *Metall. Mater. Trans. A* 36 (2005) 1515–1523, <https://doi.org/10.1007/s11661-005-0243-8>.
- [49] L. Sturz, A. Theofilatos, Two-dimensional multi-scale dendrite needle network modeling and x-ray radiography of equiaxed alloy solidification in grain-refined Al-3.5 wt-%Ni, *Acta Mater.* 117 (2016) 356–370, <https://doi.org/10.1016/j.actamat.2016.06.005>.
- [50] A. Bugno, H. Nguyen-Thi, G. Reinhardt, B. Billia, J. Baruchel, Growth and interaction of dendritic equiaxed grains: in situ characterization by synchrotron X-ray radiography, *Acta Mater.* 61 (2013) 1303–1315, <https://doi.org/10.1016/j.actamat.2012.11.008>.

- [51] C.A. Schneider, W.S. Rasband, K.W. Eliceiri, NIH Image to ImageJ: 25 years of image analysis, *Nat. Methods* 9 (2012) 671–675, <https://doi.org/10.1038/nmeth.2089>.
- [52] D.v. Alexandrov, P.K. Galenko, The shape of dendritic tips, *Philos. Trans. R. Soc. A Math. Phys. Eng. Sci.* 378 (2020), <https://doi.org/10.1098/rsta.2019.0243>.
- [53] B. Beausir, J.J. Fundenberger, Analysis tools for electron and X-ray diffraction, in: ATEX - Software. Université de Lorraine-Metz, Analysis Tools for Electron and X-Ray Diffraction, ATEX - Software, 2017. www.atex-software.eu.
- [54] M., Humbert, F. Wagner, H. Moustahfid, C. Esling, Determination of the orientation of a parent [beta] grain from the orientations of the inherited [alpha] plates in the phase transformation from body-centred cubic to hexagonal close packed, *J. Appl. Crystallogr.* 28 (1995) 571–576.
- [55] R.C. Sales, P.F. Junior, K.G. Paradelo, W.J.L. Garção, A.F. Ferreira, Effect of solidification processing parameters and silicon content on the dendritic spacing and hardness in hypoeutectic Al-Si alloys, *Mater. Res.* 21 (2018), <https://doi.org/10.1590/1980-5373-MR-2018-0333>.
- [56] C.D. Ridgeway, C. Gu, A.A. Luo, Predicting primary dendrite arm spacing in Al-Si-Mg alloys: effect of Mg alloying, *J. Mater. Sci.* (2019), <https://doi.org/10.1007/s10853-019-03558-w>.
- [57] T. Okamoto, K. Kishitake, Dendritic structure in unidirectionally solidified aluminium, tin, and zinc base binary alloys, *J. Cryst. Growth* 29 (1975), [https://doi.org/10.1016/0022-0248\(75\)90217-1](https://doi.org/10.1016/0022-0248(75)90217-1).
- [58] D.D. Reeves, T.Z. Kattamis, A model for isothermal coarsening, *Scripta Metall.* 5 (1971) 223–230, [https://doi.org/10.1016/0036-9748\(71\)90013-5](https://doi.org/10.1016/0036-9748(71)90013-5).
- [59] Q.C. Jiang, C.L. Xu, H.Y. Wang, J.G. Wang, Y.F. Yang, Estimation of the shifting distance of the eutectic point in hypereutectic Al-Si alloys by the lever rule, *Scr. Mater.* 56 (2007) 329–332, <https://doi.org/10.1016/j.scriptamat.2006.11.023>.
- [60] F. Czerwinski, Cerium in aluminum alloys, *J. Mater. Sci.* 55 (2020) 24–72, <https://doi.org/10.1007/s10853-019-03892-z>.
- [61] F. Czerwinski, B.S. Amirkhiz, On the Al-Al11Ce3 eutectic transformation in aluminum-cerium binary alloys, *Materials* 13 (2020) 1–27, <https://doi.org/10.3390/ma13204549>.
- [62] F. Vnuk, M. Sahoo, R. Van De Merwe, R.W. Smith, The hardness of Al-Si eutectic alloys, *J. Mater. Sci.* 14 (1979) 975–982, <https://doi.org/10.1007/BF00550730>.
- [63] S. Khan, A. Ourdjini, Q.S. Hamed, M.A.A. Najafabadi, R. Elliott, Hardness and mechanical property relationships in directionally solidified aluminium-silicon eutectic alloys with different silicon morphologies, *J. Mater. Sci.* 28 (1993) 5957–5962, <https://doi.org/10.1007/BF00365208>.
- [64] P. Zhang, S.X. Li, Z.F. Zhang, General relationship between strength and hardness, *Mater. Sci. Eng.* 529 (2011) 62–73, <https://doi.org/10.1016/j.msea.2011.08.061>.
- [65] I. Baker, F. Meng, Lamellar coarsening in Fe28Ni18Mn33Al21 and its influence on room temperature tensile behavior, *Acta Mater.* 95 (2015) 124–131, <https://doi.org/10.1016/j.actamat.2015.05.006>.
- [66] M. Gündüz, H. Kaya, E. Çadırli, A. Özmen, Interflake spacings and undercoolings in Al-Si irregular eutectic alloy, *Materials Science and Engineering: A* 369 (2004) 215–229, <https://doi.org/10.1016/j.msea.2003.11.020>.
- [67] I. Toda-Caraballo, E.I. Galindo-Nava, P.E.J. Rivera-Díaz-Del-Castillo, Understanding the factors influencing yield strength on Mg alloys, *Acta Mater.* 75 (2014) 287–296, <https://doi.org/10.1016/j.actamat.2014.04.064>.
- [68] J.C.F. Millett, S.J. Fensin, G.D. Owen, B.P. Eftink, C. Lear, G. Whiteman, G.T. Gray, The mechanical and microstructural response of single crystal aluminium to one dimensional shock loading: the effects of orientation, *Acta Mater.* 246 (2023), <https://doi.org/10.1016/j.actamat.2023.118727>.
- [69] W. F. Hosford, R. L. Fleischer, W. A. Backofen, Tensile deformation of aluminum single crystals at low temperatures, *Acta Metall.* 8 (1960) 187–199, [https://doi.org/10.1016/0001-6160\(60\)90127-9](https://doi.org/10.1016/0001-6160(60)90127-9).
- [70] J.H. Wu, W.Y. Tsai, J.C. Huang, C.H. Hsieh, G.R. Huang, Sample size and orientation effects of single crystal aluminum, *Materials Science and Engineering: A* 662 (2016) 296–302, <https://doi.org/10.1016/j.msea.2016.03.076>.
- [71] D. Zhou, H. Wang, D.W. Saxey, O. Muránsky, H. Geng, W.D.A. Rickard, Z. Quadir, C. Yang, S.M. Reddy, D. Zhang, Hall-Petch slope in ultrafine grained Al-Mg alloys, *Metall. Mater. Trans. A Phys. Metall. Mater. Sci.* 50 (2019) 4047–4057, <https://doi.org/10.1007/s11661-019-05329-3>.
- [72] R.L. Fleischert, Substitutional solution hardening, *Acta Metall.* 11 (1963) 203–208, [https://doi.org/10.1016/0001-6160\(63\)90213-X](https://doi.org/10.1016/0001-6160(63)90213-X).
- [73] D. Tabor, The hardness of solids, *Rev. Phys. Technol.* 1 (1970) 145–179.
- [74] M. Liu, H. Fu, C. Xu, W. Xiao, Q. Peng, H. Yamagata, C. Ma, Precipitation kinetics and hardening mechanism in Al-Si solid solutions processed by high pressure solution treatment, *Materials Science and Engineering: A* 712 (2018) 757–764, <https://doi.org/10.1016/j.msea.2017.12.033>.
- [75] Hisao Mii, Senoo Masafumi, Fujishiro Ikuya, Solid solubility of Si in Al under high pressure, *Jpn. J. Appl. Phys.* 15 (1975) 777–783, <https://doi.org/10.1143/JJAP.15.777>.
- [76] G. Mann, J.R. Griffiths, C.H. Cáceres, Hall-Petch parameters in tension and compression in cast Mg-Zn alloys, *J. Alloys Compd.* (2004) 188–191, <https://doi.org/10.1016/j.jallcom.2003.12.052>.
- [77] H. Yu, C. Li, Y. Xin, A. Chapuis, X. Huang, Q. Liu, The mechanism for the high dependence of the Hall-Petch slope for twinning/slip on texture in Mg alloys, *Acta Mater.* 128 (2017) 313–326, <https://doi.org/10.1016/j.actamat.2017.02.044>.
- [78] H. Yu, Y. Xin, M. Wang, Q. Liu, Hall-Petch relationship in Mg alloys: a review, *J. Mater. Sci. Technol.* 34 (2018) 248–256, <https://doi.org/10.1016/j.jmst.2017.07.022>.
- [79] Y.N. Wang, J.C. Huang, Texture analysis in hexagonal materials, *Mater. Chem. Phys.* 81 (2003) 11–26, [https://doi.org/10.1016/S0254-0584\(03\)00168-8](https://doi.org/10.1016/S0254-0584(03)00168-8).
- [80] B. Guan, Y. Xin, X. Huang, P. Wu, Q. Liu, Quantitative prediction of texture effect on Hall-Petch slope for magnesium alloys, *Acta Mater.* 173 (2019) 142–152, <https://doi.org/10.1016/j.actamat.2019.05.016>.
- [81] Y. Wang, H. Choo, Influence of texture on Hall-Petch relationships in an Mg alloy, *Acta Mater.* 81 (2014) 83–97, <https://doi.org/10.1016/j.actamat.2014.08.023>.
- [82] W. Yuan, S.K. Panigrahi, J. Su, R.S. Mishra, Influence of grain size and texture on Hall - Petch relationship for a magnesium alloy, *Scr. Mater.* 65 (2011) 994–997, <https://doi.org/10.1016/j.scriptamat.2011.08.028>.
- [83] Y.N. Wang, C.I. Chang, C.J. Lee, H.K. Lin, J.C. Huang, Texture and weak grain size dependence in friction stir processed Mg-Al-Zn alloy, *Scr. Mater.* 55 (2006) 637–640, <https://doi.org/10.1016/j.scriptamat.2006.06.005>.
- [84] A. Godon, J. Creus, S. Cohendoz, E. Conforto, X. Feugas, P. Girault, C. Savall, Effects of grain orientation on the Hall-Petch relationship in electrodeposited nickel with nanocrystalline grains, *Scr. Mater.* 62 (2010) 403–406, <https://doi.org/10.1016/j.scriptamat.2009.11.038>.
- [85] F. Gonzales, M. Rappaz, Dendrite growth directions in aluminum-zinc alloys, *Metall. Mater. Trans. A* 37 (2006) 2797–2806, <https://doi.org/10.1007/BF02586112>.
- [86] J. Friedli, J.L. Fife, P. Di Napoli, M. Rappaz, Dendritic growth morphologies in Al-Zn alloys - Part I: X-ray tomographic microscopy, in: *Metall Mater Trans A Phys Metall Mater Sci*, 2013, pp. 5522–5531, <https://doi.org/10.1007/s11661-013-1912-7>.
- [87] M. Becker, J.A. Dantzig, M. Kolbe, S.T. Wiese, F. Kargl, Dendrite orientation transition in Al-Ge alloys, *Acta Mater.* 165 (2019) 666–677, <https://doi.org/10.1016/j.actamat.2018.12.001>.